Numerical simulation of a turbulent hydraulic jump: Characterization of the free interface and large bubble structure

By M. Mortazavi, V. Le Chenadec † and A. Mani

1. Motivation and objectives

Bubble generation is a ubiquitous and complex phenomenon occurring as a result of non-linear behavior of the free surfaces. Plunging breakers, spilling breakers and plunging jets are just a few scenarios where bubble generation occurs. Due to its complexity and our lack of complete understanding of this phenomenon, the models developed in the literature are far from being predictive (Moraga *et al.* 2008) (Ma *et al.* 2011). In addition to macro-bubble generation another mechanism has been discovered by Sigler & Mesler (1990), which generates micro bubbles, bubbles which are generated as a result of impact of two interfaces. A thin air film is trapped in a gap between the surfaces at impact. This thin film becomes unstable and fragments into tens to hundreds of micro bubbles (Thoroddsen *et al.* 2012). The sizes of these bubbles are in the range of tens to hundreds of microns. One important instance of bubble generation is near the ship hulls, where turbulent boundary layer interactions with the free surface result in a large amount of macro and micro bubble entrainment. Due to their dominant buoyancy forces, large bubbles come to the interface and leave the domain much faster than micro bubbles. Micro bubbles stay under the interface for a long time and leave a trail behind the ships. Due to the complexity of this problem, we have considered a simpler case of a hydraulic jump, where turbulence interactions with a free surface generating a continuous stream of wave breaking. In this work we aim to understand the structure of the interface, the length scales associated with them, and the local shape of the interface. Finally, we assess whether micro-bubble generation is plausible in this scenario. Pumphrey & Elmore (1990) have characterized different bubble-generation scenarios for the case of a drop impacting a flat surface, parameterized on the drop diameter and impact velocity. Based on this study, we can assess whether the impact phenomena occurring in a turbulent hydraulic jump are prone to producing micro bubbles. A hydraulic jump with a Froude number of 2 and a Reynolds number of 11000, based on inlet height and velocity, is simulated with the physical density ratio of 831 after an experiment by Murzyn *et al.* (2005). Large bubbles are observed to form in a patch structure with the specific frequency matching the peak in the velocity energy spectrum.

2. Problem set up

2.1. *Governing equations*

The governing equations for incompressible two-phase flows include continuity and balance of momentum,

$$\boldsymbol{\nabla} \cdot \mathbf{u} = 0$$

† Aerospace Engineering Department, University of Illinois at Urbana-Champaign

$$\frac{\partial \mathbf{u}}{\partial t} + \mathbf{u} \cdot \nabla \mathbf{u} = -\frac{\nabla p}{\rho} + \frac{1}{\rho} \boldsymbol{\nabla} \cdot (\mu[\nabla \mathbf{u} + \nabla^T \mathbf{u}]) + \mathbf{g} + \mathbf{f}_{ST},$$

where $\mathbf{u}$, p, ρ, μ, $\mathbf{g}$ and $\mathbf{f}_{ST}$ are velocity, pressure, density, dynamic viscosity, gravitational acceleration and surface tension force, respectively. Second-order accurate central differencing is used on a structured uniform mesh to discretize the equations in space, and a second-order Adams-Bashforth scheme is used to discretize the equations in time. The Ghost Fluid Method is used for applying the surface tension force (Fedkiw *et al.* 1999). In order to advect the interface a geometric Volume of Fluid (VOF) method is used (Le-Chenadec & Pitsch 2013), The equation governing the VOF reads,

$$\frac{\partial f}{\partial t} + \mathbf{u} \cdot \nabla f = 0. \tag{2.1}$$

In the context of incompressible flows, the velocity divergence vanishes and we can write Eq. (2.1) as

$$\frac{D_m}{D_m t} \int_{\Omega_m} f d\mathbf{x} = 0, \tag{2.2}$$

where D_m represents the material derivative and Ω_m is the control volume over which the VOF is defined, i.e., grid cell. In addition to the VOF, a Level Set (LS) is also tracked in order to be used for accurate curvature and normal calculations,

$$\frac{\partial G}{\partial t} + \mathbf{u} \cdot \nabla G = 0.$$

A third-order accurate WENO scheme is used for Level Set time advection. In order to make the two solutions of VOF and LS consistent, the level set is modified by a distance function constructed from the VOF field at each time step. Details of the numerical procedures can be found in Le-Chenadec & Pitsch (2013).

2.2. *Computational domain and boundary conditions*

Our simulation is based on the experiment of Murzyn *et al.* (2005). The inflow Froude number, based on the inflow height and velocity, is 2. The inflow water height is $h = 5.9$ cm and the inflow velocity is 1.5 m s^{-1}. The Reynolds number is 11000 and the Weber number is 1866. The domain length size is chosen to be large, $20h \times 4h \times 4h$ (*length × height × width*), to minimize the effect of the outlet boundary condition. We have used a grid of $1280 \times 256 \times 256$ in order to have at least three grid points across the Hinze scale as reported in the experiment of Murzyn *et al.* (2005). Our Reynolds number does not match the experiment because we have artificially increased the water viscosity for stability reasons. Increasing the viscosity does not contaminate the results because the most important turbulence interaction with bubbles and interface is at the scale of the smallest bubbles (Hinze scale), which we capture with our grid, and turbulence at much smaller scales has no significant effect on bubble generation and interface dynamics. The bottom and top boundary conditions are chosen to be Neumann. Since the boundary layer thickness does not exceed 36% of the inflow height according to the experiment, its effect on the interface is not significant. The periodic boundary condition is used for the spanwise direction and a convective boundary condition for the outflow. At the outflow boundary, in addition to balancing the total flow rate, which is a necessary condition for the Poisson equation (with Neumann boundary conditions for pressure) to be well-posed, we ensure that the water flow rate balances with the inflow water flow rate. Both water and air flow rates are balanced by letting the air flow in or out at a small section of the
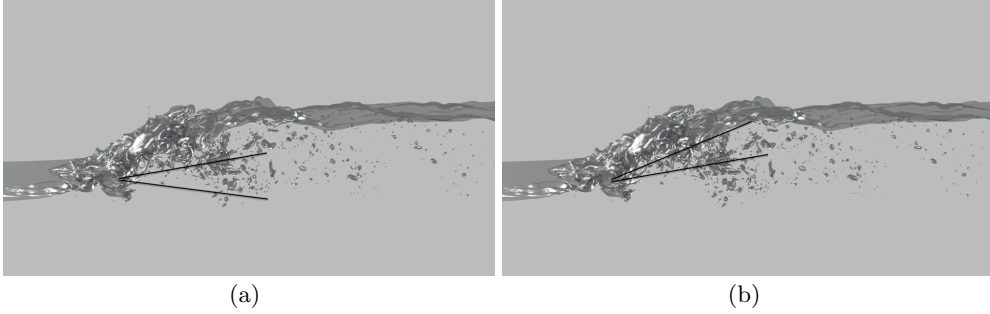
(a)   (b)

FIGURE 1. Two regions in a hydraulic jump with different bubble generation mechanisms and void fraction characteristics.(a) Lower region of the jump (turbulent shear region). (b) Upper region of the jump (roll-up region).

outflow boundary. This treatment does not affect the flow inside the domain nor does it affect the stability of the code. The inflow boundary condition is uniform for the water and is a sharp 1D Blasius divergence-free velocity profile for the air side.

3. Validation

3.1. *Bubble generation*

There are two regions of bubble generation with different characteristics, as argued by Murzyn *et al.* (2005). Figure 1 shows these two regions. The lower region, Figure 1(a), is characterized by an advection-diffusion process, and the interaction of the interface is minimal in this region. Therefore, the bubbles generated at the toe are convected and diffused downstream of the flow. According to Chanson (1996), the void fraction in this region can be expressed as a Gaussian profile, which is the solution to a steady advection-diffusion process,

$$C = C_{max} \exp\left[-\frac{1}{4}\frac{U}{D}\frac{(z - z_{Cmax})^2}{x} \right],$$ (3.1)

where x, C_{max}, U, D and z_{Cmax} are, respectively, stream-wise location, maximum void fraction, characteristic velocity, effective diffusivity and vertical location of the maximum void fraction, all at the particular x location. Murzyn *et al.* (2005) also showed that their results follow a Gaussian profile with appropriate coefficients, which they report in the experiment.

We compare our time and span-wise averaged void fraction, C, to the experiment, as a function of the similarity variable $(U/4xD)^{1/2}(z - z_{Cmax})$ in Figure 2. The simulation results agree with the experiment very well, and we can see the self-similar behavior of the void fraction in the lower region of the hydraulic jump.

The upper region is a result of interfacial aeration as argued by Murzyn *et al.* (2005), and a good fit to the void fraction is found by Brattberg *et al.* (1998), and is in the form of an error function (Eq. (3.2)),

$$C = \frac{1}{2}\mathrm{erf}\left(\frac{z - z_{C50}}{2\sqrt{Dx/U}} \right),$$ (3.2)
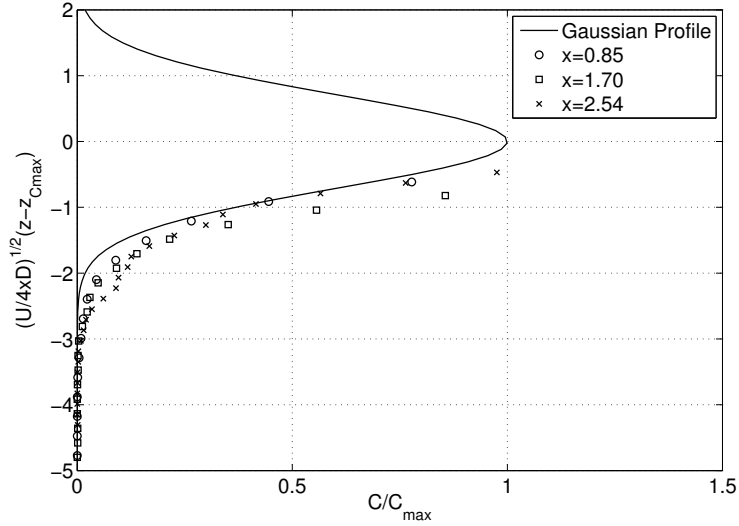
FIGURE 2. Simulation results of void fraction in the lower region of a hydraulic jump for different stream-wise locations compared with the theoretical and experimentally validated Gaussian profile (Murzyn *et al.* 2005).
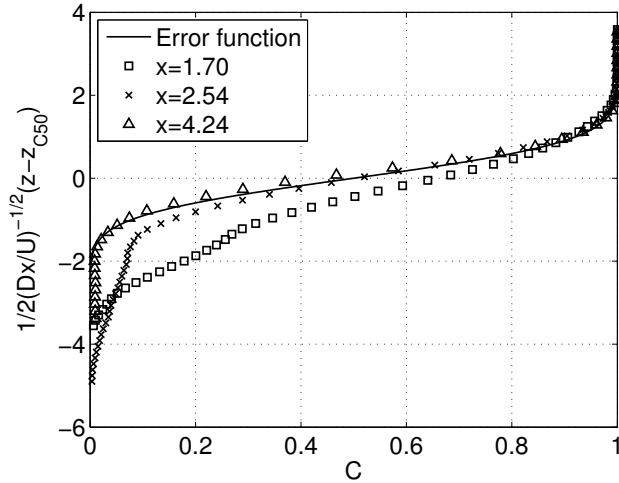

FIGURE 3. Simulation results of void fraction in the upper region of a hydraulic jump for different stream-wise locations compared with the experimentally suggested error function of Eq (3.2), (Murzyn *et al.* 2005).

where z_{C50} is the vertical position for which the void fraction equals one half. The void fraction is not normalized in this case since the maximum value is one in the air side.

Similarly, by using the values for the z_{C50} and D/Uh from the experiment, we compare the simulation results with the suggested fit in Eq. (3.2) in Figure 3. The value of z_{C50} used for the plot comes from the simulation itself. We notice a discrepancy of at most 30% between the value of z_{C50} in the simulation and experiment, which may be due
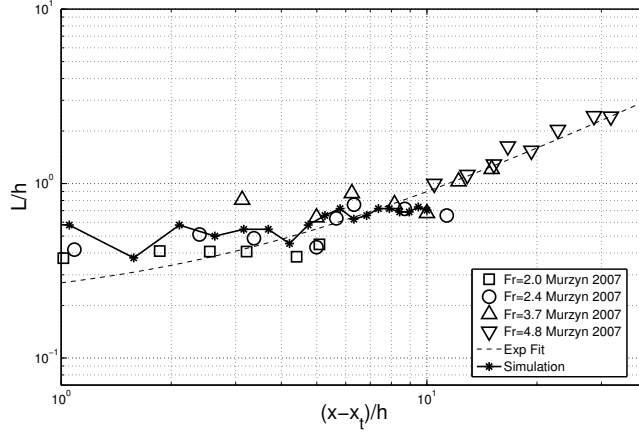
FIGURE 4. Simulation results of interface length scale compared with the experiment (Murzyn *et al.* 2007).

to lack of statistical convergence of the void fraction in the upper region. Nevertheless, the void fraction in the upper region follows the trend of the error function proposed by Murzyn *et al.* (2005) in Eq. (3.2).

3.2. *Interface length scale*

The interface length scale for hydraulic jumps is another quantity that is computed by Murzyn *et al.* (2007). They define the interface length scale as the integral under the autocorrelation curve of the phase detection signal. We have used the signed distance function, which is a measure of the distance of a point from the interface, as the signal, and define the integral of its autocorrelation curve as the interface length scale. Figure 4 shows a comparison between the simulation results and the experiment. The agreement is quite good for larger values of x; however, it deviates more for smaller values of x.

4. Interface characteristics

In order to find local values of curvature and velocity, we triangulate the interface using the Marching Cubes method (Lorensen & Cline 1987). For each triangle, we can compute the two principal curvatures from the information of the LS field. In order to compute the local interface characteristics of the interface, we divide the interface into 10 windows in the steam-wise direction. Each window has a length of $2h$. In the following sections, the averages are taken over the triangles residing in a particular window.

4.1. *Interface local shape*

Bermejo-Moreno & Pullin (2008) characterized the local geometrical shapes of the turbulence structures by means of principal curvatures, k_1 and k_2. We have computed the principal curvatures on the interface for each window and have plotted their joint pdf functions in Figure 5. We can observe that the joint pdf is stretched along the two horizontal and vertical axes, an indication that the local shape of the interface is mostly cylindrical. This is an important observation of the impact process. It is important to know what kind of interfaces are impacting each other with what kind of local shapes. We can also observe that the joint pdfs have a tendency to shift to the line $k_1 = k_2$
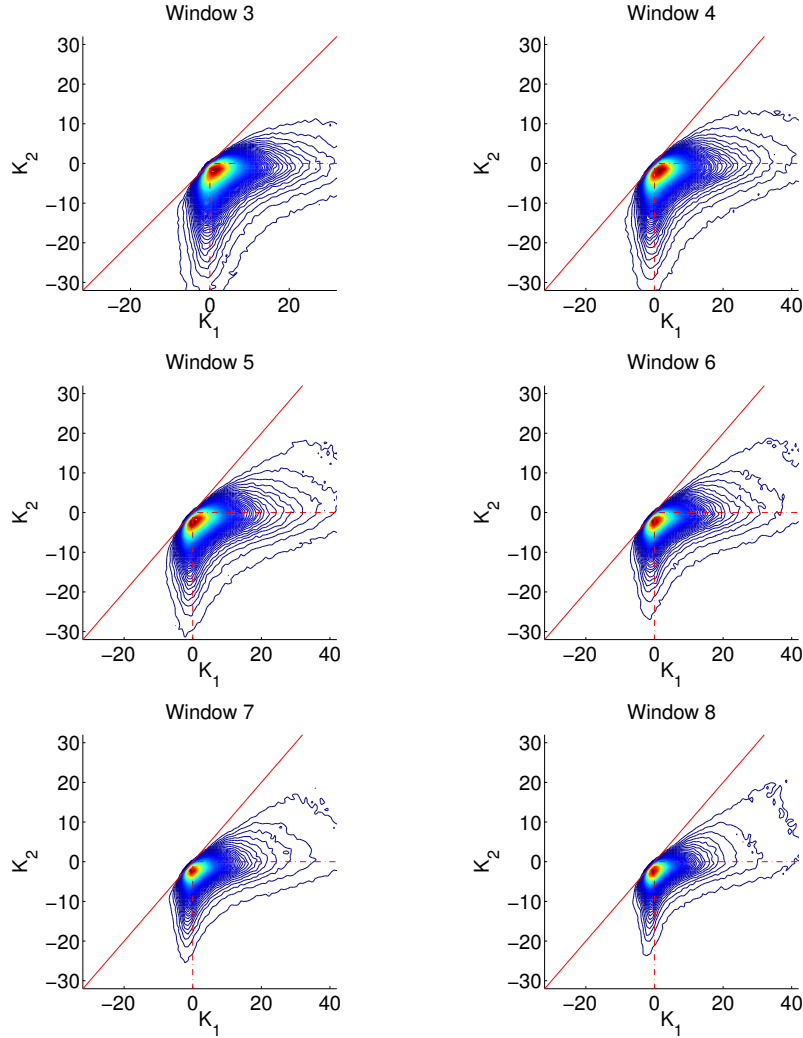
FIGURE 5. First principal curvature vs. second principal curvature on the interface for different stream-wise locations of the hydraulic jump. Each window has a length of $2h$. Window 3 starts at the toe of the jump.

for larger values of x (larger window numbers). The reason is that the area ratio of the bubbles to total area increases for those places as compared to the windows closer to the toe of the jump. Since the line of $k_1 = k_2$ is a characteristic of a spherical shape and indicates the presence of the bubbles, the contours shift towards this line for larger window numbers.

4.2. *Interface curvedness distribution*

Interface curvedness, as apparent by its name, is a measure of how much an interface is curved (Bermejo-Moreno & Pullin 2008). It also reduces the two principal curvatures to a single number, making it a convenient way to measure the local interface curvature. It is defined as the geometrical mean of the two principle curvatures,

$$C = \sqrt{\frac{\kappa_1^2 + \kappa_2^2}{2}}.$$

To gain insight into the curvedness distribution along the interface of the turbulent hydraulic jump, we have computed the Probability Density Function (PDF) of the curvedness for different positions of the jump. Figure 6 shows the PDF of the curvedness on the interface. The PDF of the curvedness is computed based on area. The sum of the area of a particular curvedness divided by the total area is a measure of probability of finding a point with that particular curvedness on the interface. The results for two different resolutions are shown in Figure 6. The solid line represents the grid of $1280 \times 256 \times 256$ and the dash-dotted line represents a mesh with half the resolution in each direction. The finer mesh resolves smaller structures, the reason why the value of the PDF for the fine mesh at larger values of curvedness is higher. The vertical dashed lines represent the values of curvedness for which the calculations of curvedness for coarse and fine grids are unreliable. The values for the maximum curvedness, according to our assessments on a canonical case of a sphere, are set to $1.5/\Delta x$. Interestingly, we can observe a power law distribution for the PDFs with the slope of $-5/3$ which extends for a long range.

4.3. *Potential interface impact and micro-bubble generation*

Pumphrey & Elmore (1990) have studied different types of bubble generation for the case of a droplet impacting a flat surface of the same liquid. They have organized their observations into a plot, which is shown in Figure 7. Droplet diameter and impact velocity are the parameters which determine the type of bubble generation. Micro-bubble generation is observed to occur for relatively low velocities. In this study, in Figure 8, we have plotted the joint PDF of the velocity fluctuations from the mean value at the interface and the equivalent diameter corresponding to the interface. Since we know that the local shape of the interface is mostly cylindrical, the local equivalent diameter can be defined based on the curvedness as $D = \sqrt{2}/C$. The joint PDF shows that if impact happens on the interface, based on the relative velocity of the two impacting interfaces (characterized by the velocity fluctuations) and their shape (characterized by the equivalent diameter), there is a strong likelihood that micro-bubble generation occurs, in the domain. Experimental observations of micro-bubble generation are also plotted on top of simulation results in Figure 8.

5. Large bubble formation structure

5.1. *Velocity energy spectrum and connection with bubble generation*

The energy spectra of the three components of velocity are computed as a function of frequency for three locations of the jump, $x/h = 6, 8, 10$, shown in Figures 9-11. We averaged the spectra in the periodic span-wise direction. Two grid resolutions are compared. The fine grid of $1280 \times 256 \times 256$ is compared with the results of the coarse grid, which has half the grid resolution in each direction. The slope of $-5/3$ is observed in the inertial range of the turbulence spectrum. Liu *et al.* (2004) have also reported on the spectrum of their hydraulic jump experiments, and they have also observed the $-5/3$ slope. Note that the Kolmogorov energy cascade assumption to smaller scales is also valid for highly bubbly two-phase flows.

Another interesting observation from the energy spectrum profiles is that a distinctive frequency is recognizable, especially for the vertical velocity component, which is believed
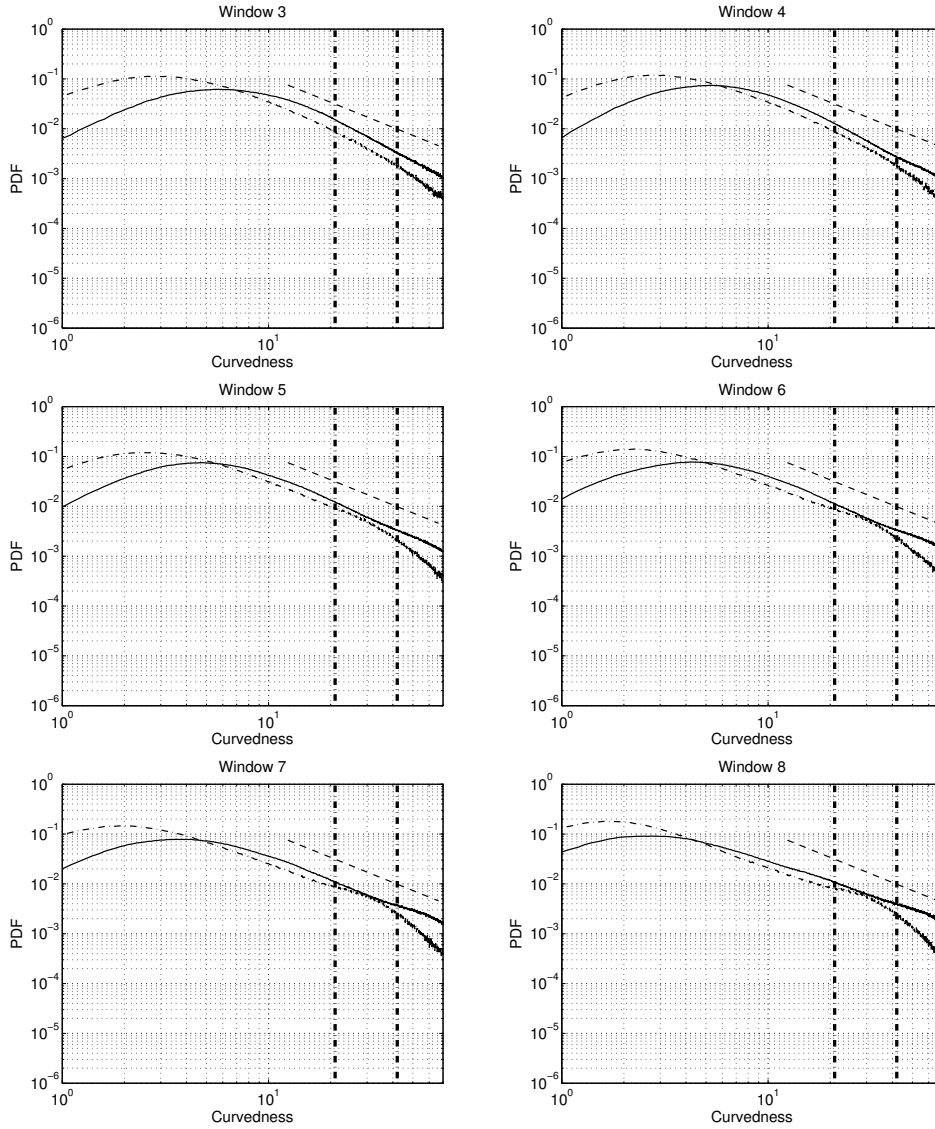
FIGURE 6. Interface curvedness PDF for different locations of the jump. Each window has a length of $2h$ and window 3 starts at the toe of the jump. Solid line: fine grid, dash-dotted line: coarse grid, dotted line: slope of $-5/3$, and vertical dashed line: values of curvedness after which the simulation results are not reliable (computed as $1.5/\Delta x$).

to be the result of the bubble-generation mechanism and the structure of the flow. These peaks are at frequencies of $3.47Hz$ and $3.97Hz$ for locations $x/h = 8$ and $x/h = 10$, respectively, which correspond to non-dimensional Srtouhal numbers of $S = fh/U_1 = 0.136$ and $S = fh/U_1 = 0.156$.

5.2. *Large bubble-patch structure*

Visual observations of bubble generation suggest that the large bubbles are generated in a patch-structure pattern and are generated periodically (Figure 12). Therefore, there is
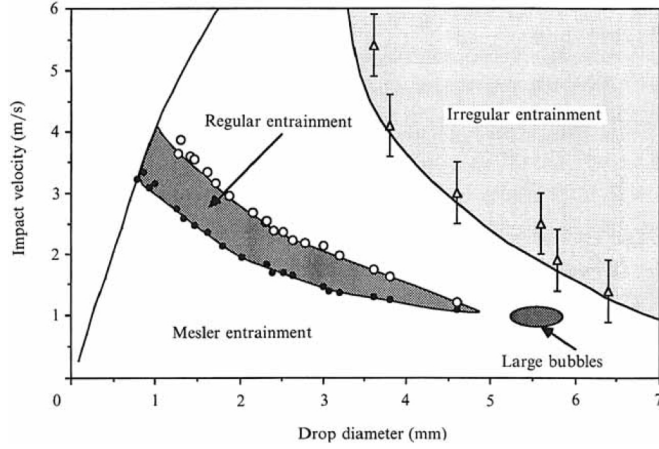
FIGURE 7. Pumphrey diagram of bubble generation for droplet impact on a flat surface of the same liquid, Pumphrey & Elmore (1990).
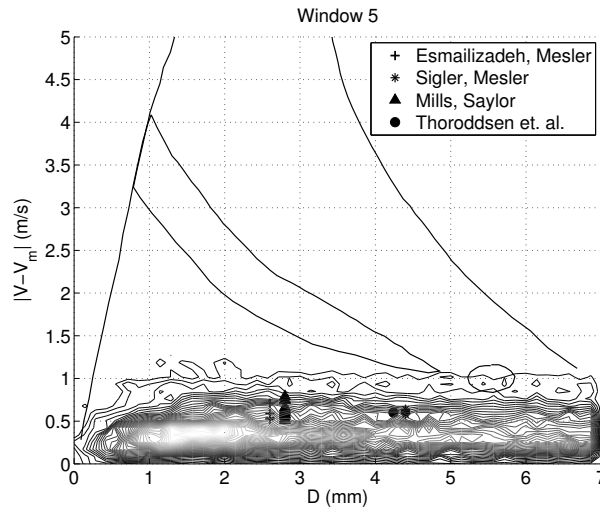

FIGURE 8. Joint PDF of velocity fluctuations on the interface and interface equivalent diameter computed from the curvedness $D = \sqrt{2}/C$.

an intrinsic frequency associated with this bubble-patch generation. In order to quantify this frequency we have divided the domain into 100 sections and computed the void fraction in each section as a function of time. Figure 13(a) shows this void fraction signal for the interval of $8.8 < x/h < 9.0$. This interval was chosen because it is neither too close to the jump toe, where the bubble patches are still not fully formed, not too far from it, where the bubbles are too dissipated and the void fraction signal becomes faded and the frequency is not recognizable. Figure 13(b) shows the autocorrelation of the signal as computed from Eq. (5.1).

$$R_V(\Delta t) = \frac{\int_0^T V_b(t)V_b(t + \Delta t)dt}{\int_0^T V_b(t)V_b(t)dt}. \tag{5.1}$$
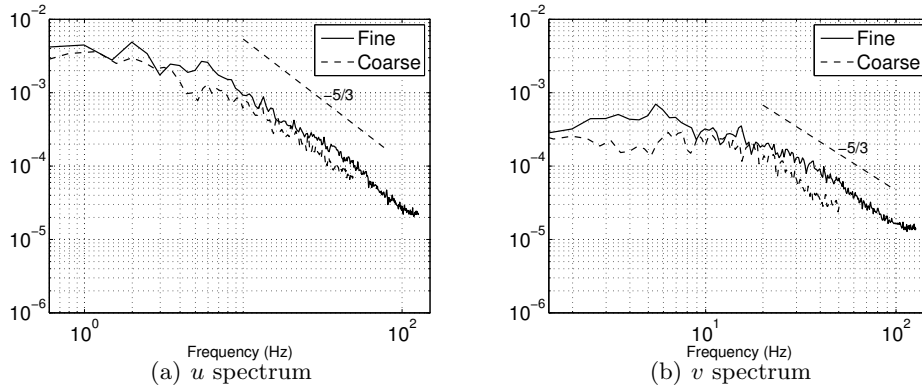
FIGURE 9. Energy spectrum of velocity components for $x/h = 6$.
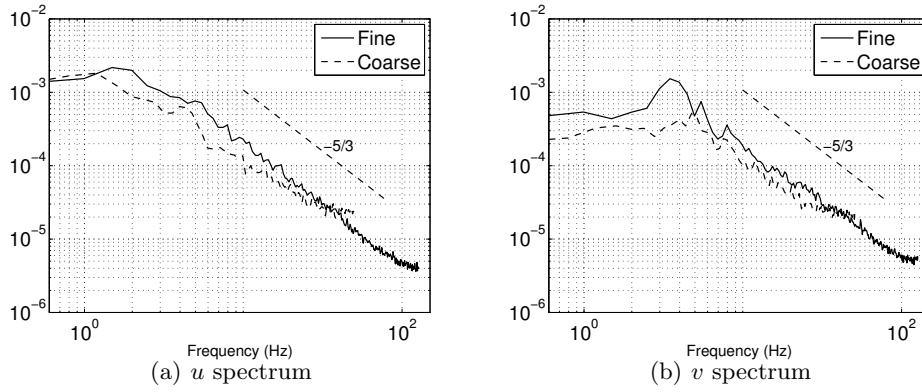
FIGURE 10. Energy spectrum of velocity components for $x/h = 8$.
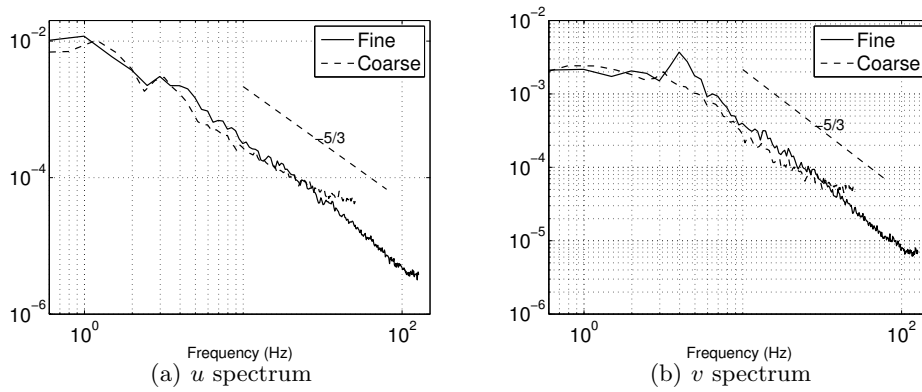
FIGURE 11. Energy spectrum of velocity components for $x/h = 10$.

The autocorrelation plot shows the periodic behavior of the void fraction signal. The period can be determined from the first peak of the plot, which occurs for non-dimensional
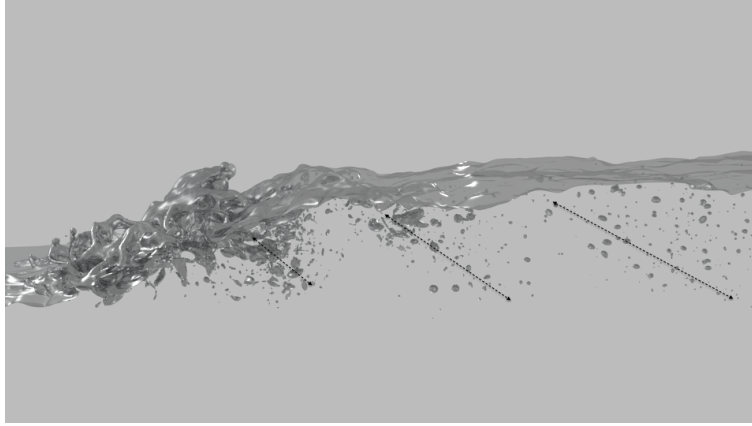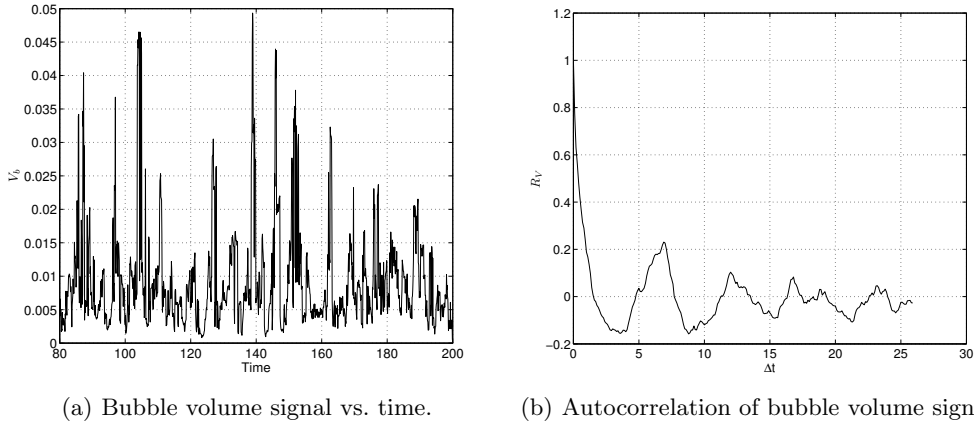
FIGURE 12. Bubble patches generated periodically and convected downstream with non-dimensional frequency of S $= fh/U_1 = 0.145$.

(a) Bubble volume signal vs. time.

(b) Autocorrelation of bubble volume signal.

FIGURE 13. Bubble volume signal and its normalized autocorrelation, for a region of $8.8 < x/h < 9.0$. The autocorrelation plot shows a periodic behavior of bubble patches passing through the domain. The non-dimensional Strouhal number associated with this phenomenon is S $= fh/U_1 = 0.145$.

$\Delta t = 6.9$. The non-dimensional frequency associated with that is S $= fh/U_1 = 0.145$. The Strouhal number obtained from the energy spectrum peak has less than 8% error relative to the observed bubble patch non-dimensional Strouhal number. From this observation we conclude that the nature of bubble generation has a footprint in the velocity spectrum and shows itself as a dominant frequency, which is especially observable in the spectrum of the vertical component of velocity. Liu *et al.* (2004) also observed a peak in their velocity spectrum at frequency of $f = 3.7Hz$, which corresponds to S $= fh/U_1 = 0.157$. This value also matches well with our calculations.

6. Conclusion

In this paper we have discussed the interface local shape and curvedness distributions of a turbulent hydraulic jump with a Froude number of 2, Reynolds number of 11000 and

Weber number of 1866, following the experiment of Murzyn *et al.* (2005). We compared the void fraction and interface length scale with the experimental results, which showed good agreement between them. We have observed that the impact events on the interface have a strong likelihood of generating micro bubbles based on the experimental observations of Pumphrey & Elmore (1990). Velocity energy spectra for different stream-wise locations of the hydraulic jump were computed. A $-5/3$ power law is observed in the inertial range and the presence of a dominant peak is noticed. This dominant frequency is associated with the bubble-generation mechanism. The frequency of the peak matches with the frequency of the bubble-patch generation.

REFERENCES

Bermejo-Moreno, I. & Pullin, D. I. 2008 On the non-local geometry of turbulence. *J. Fluid Mech.* **603**, 101–135.

Brattberg, T., Toombes, L. & Chanson, H. 1998 Developing air-water shear layers of two-dimensional water jets discharging into air. *ASME Fluids Engineering Division Summer Meeting*.

Chanson, H. 1996 *Air Bubble Entrainment in Free Surface Turbulent Flows*. Academic Press.

Fedkiw, R., Aslam, T., Merriman, B. & Osher, S. 1999 A non-oscillatory eulerian approach to interfaces in multi material flows (the ghost fluid method). *J. Comput. Phys* **152**, 457–492.

Le-Chenadec, V. & Pitsch, H. 2013 A 3d unsplit forward/backward volume-of-fluid approach and coupling to the level set method. *J. Comput. Phys* **233**, 10–33.

Liu, M., Rajaratnam, N. & Zhu, D. Z. 2004 Turbulence structure of hydraulic jumps of low froude numbers. *J. Hydraul. Eng.* **130**, 511–520.

Lorensen, W. E. & Cline, H. E. 1987 Marching cubes: a high resolution 3d surface contraction algorithm. *ACM SIGGRAPH Computer Graphics* **21**, 163–169.

Ma, J., Oberai, A. A., Jr, R. T. L. & Drew, D. A. 2011 Modeling air entrainment and transport in a hydraulic jump using two-fluid rans and des turbulence models. *Heat Mass Transfer.* **47**, 911–919.

Moraga, F., Carrica, P., Drew, D. & Jr, R. L. 2008 A sub-grid air entrainment model for breaking bow waves and naval surface ships. *Comput. & Fluids* **37**, 281–298.

Murzyn, F., Mouaze, D. & Chaplin, J. 2005 Optical fibre probe measurements of bubbly flow in hydraulic jumps. *Int. J. Multiphase Flow* **31**, 141–154.

Murzyn, F., Mouaze, D. & Chaplin, J. 2007 Air-water interface dynamic and free surface features in hydraulic jumps. *J. Hydraul. Res.* **45**, 679–685.

Pumphrey, H. C. & Elmore, P. A. 1990 The entrainment of bubbles by drop impacts. *J. Fluid Mech.* **220**, 539–567.

Sigler, J. & Mesler, R. 1990 The behavior of the gas film formed upon drop impact with a liquid surface. *J. Colloid Interf. Sci.* **134**, 459–474.

Thoroddsen, S., Thoraval, M., Takehara, K. & Etoh, T. 2012 Micro-bubble morphologies following drop impacts onto a pool surface. *J. Fluid Mech.* **708**, 469–479.